Materials and Design 145 (2018) 88–96

Contents lists available at ScienceDirect

Materials and Design

journal homepage: www.elsevier.com/locate/matdes

Development of a novel TiNbTa material potentially suitable for bone replacement implants

E. Chicardi [a,b,*], C.F. Gutiérrez-González [c], M.J. Sayagués [d], C. García-Garrido [d,**]

[a] Departamento de Ingeniería Metalúrgica y de Materiales, Universidad Técnica Federico Santa María, Av. España 1680, Valparaíso, Chile
[b] Departamento de Ingeniería y Ciencia de los Materiales y del Transporte, Camino de los Descubrimientos, s/n, 41092 Sevilla, Spain
[c] Centro de Investigación en Nanomateriales y Nanotecnología (CINN) [Consejo Superior de Investigaciones Científicas (CSIC), Universidad de Oviedo, Principado de Asturias], Avda. de la Vega, 4 – 6, 33940 El Entrego, Spain
[d] Instituto de Ciencia de Materiales de Sevilla (ICMSE-CSIC), Américo Vespucio 49, 41092, Sevilla, Spain

HIGHLIGHTS

- An original submicrometric (β + γ)-TiNbTa material was successfully developed.
- It was obtained via a combined Low Energy Mechanical Alloying and Pulsed Electric Current Sintering metallurgical process.
- It was determined a novel *fcc* structure for Ti alloys (γ-TiNbTa alloy).
- This material possesses a low Young's modulus and an outstanding yield strength.
- This would allow obtaining (β + γ)-TiNbTa foams without mechanical strength damage.

GRAPHICAL ABSTRACT

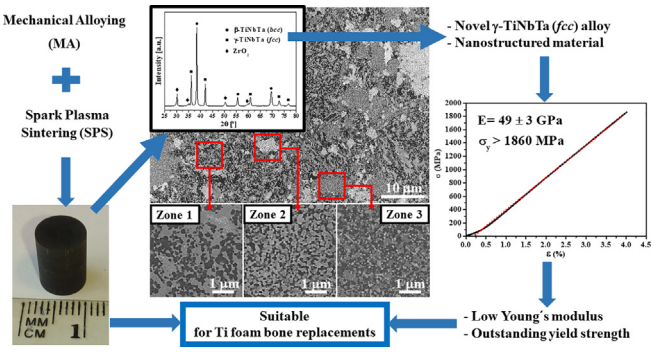

ARTICLE INFO

Article history:
Received 22 December 2017
Received in revised form 13 February 2018
Accepted 14 February 2018
Available online 17 February 2018

Keywords:
Ti alloys
Biomaterial
Yield strength
Young's modulus
Stress-shielding
Bone replacement implants

ABSTRACT

A novel (β + γ)-TiNbTa alloy has been developed by a combined low energy mechanical alloying (LEMA) and pulsed electric current sintering process (PECS). Microstructurally, this material presents interesting characteristics, such as a submicrometric range of particle size, a body-centered phase (β-TiNbTa) and, mainly, a novel face-centered cubic Ti-based alloy (γ-TiNbTa) not previously reported. Related to mechanical performance, the novel (β + γ)-TiNbTa shows a lower E (49 ± 3 GPa) and an outstanding yield strength (σ_y > 1860 MPa). This combination of original microstructure and properties makes to the (β + γ)-TiNbTa a novel material potentially suitable as biomaterial to fabricate bone replacement implants, avoiding the undesirable and detrimental *stress-shielding* problem and even the usual damage on the mechanical strength of Ti-based foams biomaterials.

1. Introduction

Commercially pure titanium (c.p. Ti grade 4) and the Ti6Al4V alloy (Ti grade 5), ASTM B265–10, are the most widely metallic materials used for bone replacements implants [1]. However, they present an important disadvantage, a high Young's modulus (between 100 and

* Correspondence to: E. Chicardi, Departamento de Ingeniería Metalúrgica y de Materiales, Universidad Técnica Federico Santa María, Av. España 1680, Valparaíso, Chile.
** Corresponding author.
E-mail addresses: echicardi@us.es (E. Chicardi), cristina.garrido@icmse.csic.es (C. García-Garrido).

https://doi.org/10.1016/j.matdes.2018.02.042
0264-1275/

105 GPa [2]) in comparison with the trabecular and cortical bone (10.4–14.8 GPa and 18.6–20.7 GPa, respectively [3]). This disparity of the stiffness between the implant material and the adjacent bone is detrimental to the stability of the bone–implant ensemble. The incorrect transference of the stress supported by the bone to the implant leads to bone resorption, osteopenia, i.e., the reduction in bone density, loosening of the implant and/or premature bone fracture [4,5]. Therefore, the key aspect to avoid *stress shielding* is matching the Young's modulus of the implant to that of the bone tissue [6]. For this purpose, research efforts have mainly followed by two different routes.

The first one is the development of cellular solids or foams (porous materials) from c.p.Ti or Ti6Al4V to decrease the density and, therefore, their Young's modulus based in the well-known inverse relationship between both properties [7–9]. Potential porous Ti-based biomaterials with homogeneous-, longitudinal-, and radial-graded interconnected porosity [10,11] replicating bone structure have been developed, with E value similar to that of the cortical bone (~20 GPa). However, the high porosity needed to reach this E value compromises other important characteristic of design, such as the yield strength (σ_y) under monotonic and/or fatigue loads [12,13]. Thus, the σ_y can be diminished from the 655 and 828 MPa for bulk Ti and Ti6Al4V [14], respectively, to 87 MPa for Ti foams with 67 vol% of porosity [15] and 167–69 MPa for Ti6Al4V foams with 50–70 vol% of porosity [13]. For comparison purpose, the yield strength for cortical bone determined by compression test is 135 ± 34 MPa [16].

The second path to obtain Ti-based biomaterials with low E is focused on the development of Ti-based alloys with different structure that of the c.p. Ti and the Ti6Al4V alloy. These phases present, at room temperature, α and (α + β) structures [17], respectively. The α phase is a hexagonal close-packed (hcp) structure, while the β phase is a body-centered cubic (*bcc*) structure. It is widely reported that metastable β-Ti alloys have lower E than α-Ti alloys, but still higher than the cortical and trabecular bones [18]. The β-Ti alloys possess a unique balance of low stiffness, formability, and weldability, making them suitable for a wide range of clinical applications [19–21].

Although the metastable β-Ti is a high-temperature phase, with an α → β dimorphic allotropic transformation at transition temperature of 882 °C [22], it is possible to maintain the β-Ti thanks to the existence of some transition metals that act as β stabilizers at room temperature. The β stabilizer elements mainly include Mo, V, Nb, Ta, and Zr as β-isomorphous [23,24] and Cr, Co, Cu, Fe, and Ni as β-eutectoid elements [22,25]. The advantage of the β-isomorphous elements is the high amount of substitutional solid solution and their inability to form Ti intermetallic compounds, with high E [26–28], according to their binary phase diagrams.

Thus, based on this assertion, β-Ti alloys have been developed with Young's modulus relatively low (minimum E value of 35 GPa) [29,30] and close to that of the cortical bone (~21 GPa). However, their E still remains far from that of trabecular bone (~14 GPa). Nb, Ta, and Zr are the main alloyed elements due to their higher biocompatibility [31] and their β-isomorphous character. Also, these new β-Ti alloys present, as general trend, yield strength lower than c.p. Ti, Ti6Al4V and other first generation alloys with alfa structure. As example, the β-Ti-Nb-Ta-Zr alloys showed σ_y values between 530 and 804 MPa and the β-Ti-Nb-Sn-Mo-Zr between 668 and 825 MPa [19,32,33]. Therefore, it would not be possible to develop β-Ti alloys (bulk or foams) with an optimal combination of both low E and optimal yield strength similar to the cortical and trabecular bones.

Therefore, an alternative approach to meet the aforementioned E and σ_y requirements would be the development of amorphous and nanocrystalline alloys, or even, Ti alloys with novel structures [34]. These efforts should be directed at decreasing the E value to a level close to that of the trabecular bone and minimizing the loss of mechanical strength for porous Ti alloys. These requirements could be met by amorphous [35,36] and nanocrystalline materials, which have higher strength values as compared to other microstructured polycrystalline materials [37]. Additionally, the development of other structures for Ti alloys, such as tetragonal structure for the intermetallic γ-TiAl [38], could be another interesting approach to address stress shielding due to expected discrepancy in mechanical behavior.

Therefore, the aim of this work is to develop an amorphous and/or nanostructured Ti alloy bulk material with structure different of the traditional hcp α-Ti and *bcc* β-Ti alloys. This is expected in order to obtain an optimal product, decreasing Young's modulus (E) while increasing yield strength (σy), for use as raw material to fabricate bulk or foam bone replacement implants, without the detrimental stress-shielding behavior.

For this purpose, we employed the combined low-energy mechanical alloying (LEMA) and the pulsed electric current sintering (PECS) powder metallurgy processes. LEMA was selected for its ability to produce homogeneous materials and induce amorphization and phase transformation [39]. PECS is a sintering method that simultaneously uses high current density and pressure to consolidate materials in a short period of time, commonly seconds or minutes, due to the possibility to apply higher heating rates than conventional sintering techniques. This PECS sintering technique was selected for its ability to maintain the nanostructure and partially amorphous characteristic on the consolidated powders [40].

Two elements, Nb and Ta, were introduced to obtain a Ti-based alloy with 57Ti-30Nb-13Ta (atomic percent [at.%]) nominal composition. Both elements were selected due to their β stabilizing behavior, to ensure the absence of the α phase (due to its higher E value), biocompatibility [41,42], and ability to prevent particle increase [43]. In addition, Nb was introduced in high amounts since mechanical alloying causes it to undergo an allotropic transformation from β (*bcc*) phase to γ (*fcc*) phase [44]. We expect that this Nb transformation can induce the same transformation for the 57Ti-30Nb-13Ta (at.%) material.

2. Materials and method

Elemental powders of titanium (CAS number 7440-32-6, 99.6% purity, <325 mesh, NOAH tech, San Antonio, TX, USA), niobium (CAS number 7440-03-1, 99.9% purity, <325 mesh, NOAH tech.), and tantalum (CAS number 7440-25-7, 99.9% purity, <325 mesh, NOAH tech.), with nominal composition of 57Ti-30Nb-13Ta (at.%), were used to develop a TiNbTa potential biomaterial. The mechanical alloying process was carried out under low-energy (LEMA) conditions to prevent the grain growth that can occur in the case of ductile metals under high-energy conditions. In brief, a planetary ball mill (PM400, Retsch GmbH) was used at spinning rate of 250 rpm for the main plate and the two vials of the mill, under an argon inert gas atmosphere (H_2O ≤ 8 ppm and O_2 ≤ 2 ppm, Linde Group, Spain). Yttria-stabilized zirconia (YSZ) balls and vials were used as milling media due to their lower density in comparison with the stainless steels, which produces low-impact energy during milling. A ball-to-powder ratio (BPR) of 10 was applied. In addition, a 3 wt% of zinc stearate (CAS number 557-05-1; 99.9% purity; <325 mesh, NOAH tech.) was used as process control agent (PCA) to avoid welding and excessive particle agglomeration. It was applied for 60 h of milling time at cyclic intervals of 30 min OFF and 30 min ON, in order to reduce the temperature inside the vial. This 60 h of milling time was determined according to the milling conditions reported for similar materials in previous published works [45].

Subsequently, the as-milled TiNbTa powder was sintered by the PECS technique (FCT System GmbH. Germany. Model HPD-25) at an optimized temperature and pressure of 1400 °C and 30 MPa, respectively, based on the reduction of porosity, at a high heating rate of 500 °C·min^{-1}, with no dwell time and free cooling. High vacuum was used as work atmosphere (~10^{-6} atm). The as-sintered TiNbTa specimen was prepared with diameters of 20 mm and height of 10 mm.

The X-Ray Diffraction (XRD) patterns for as-milled and as-sintered TiNbTa specimens, latter after metallographic treatment, i.e., cutting and surface polishing (P400 grit SiC, diamond suspensions with

particles of 9 μm, 3 μm, 1 μm and, finally, a colloidal suspension of 0.05 μm of SiC particles), were collected by a PANalytical X'Pert Pro instrument. It was equipped with a Bragg-Brentano θ/2θ geometry detector, a Cu K_α radiation source (40 kV, 40 mA), a secondary Kβ filter, and an X'Celerator detector. They were obtained by scanning from 20 to 140° of 2θ°, with 0.02° steps and a counting time of 300 s·step^{-1}. Lanthanum hexaboride, LaB6 (Standard Reference Material 660b, NIST), was used to correct the instrumental error of the diffractometer and calibrate the positions of the diffraction lines. The structural elucidations of the phases and the corresponding space group symmetries (SGS) were determined by the Dicvol software, using the dichotomy method [46], and compared with the PDF-4+ database from the International Centre for Diffraction Data (ICDD).

Further, with regard to the XRD pattern of as-sintered TiNbTa specimen, a Rietveld analysis was carried out to determine the lattice parameters (a, b, c), the crystalline domain size (D), and the quantification of phases using the Fullprof software by Carvajal [47].

Scanning electron microscopy (SEM) images in secondary electron mode were obtained using a Hitachi S-4800 field at an acceleration voltage of 5 kV on the as-sintered TiNbTa specimen. The quantification of Ti, Nb, Ta, and, specifically, Zr, the latter being sourced from the milling media (ZrO_2), was carried out in each phase by point X-Ray energy dispersive spectrometry (EDS) with a detector coupled in the SEM at an acceleration voltage of 30 kV.

On the other hand, high-angle annular dark-field (HAADF) images as well as point and mapping EDS were obtained in scanning transmission electron microscopy (STEM) mode by using FEI Talos™ F200S scanning/transmission electron microscope at an acceleration voltage of 200 kV (point resolution = 0.25 nm). In turn, the selected area electron diffraction (SAED) patterns for the different phases detected were collected in TEM mode on a disc of the as-sintered specimen with diameter 3 mm, which was prepared by cutting, polishing (similar than previously exposed), dimpling, and ion milling (DuoMiller, Gatan Inc. and ion miller model no. 1010, Fischione), successively. The JEMS software was used to resolve the structures obtained by SAED.

Finally, the elastic behavior of the as-sintered TiNbTa specimen at room temperature was determined by a compression test in a universal mechanical testing machine (Instron mod. 6025). The tests were carried out according to the ASTM E9-09 standard, with displacement rate of 0.05 mm/min and a maximum application load of 100 kN, the maximum value available for the machine. Thus, five cylindrical specimens with a diameter 8 mm and height 10 mm (diameter/height rate equal to 0.8), as recommended for "*short solid cylindrical specimens*" in the ASTM E9-09, were tested. These specimens were obtained from the abovementioned cylinders (ϕ = 20 mm and h = 10 mm) by wire electroerosion process (EDM, *Electrical Discharge Machining*). The absence of oxygen on the surface of the machined cylinders was corroborated by point SEM-EDS. Finally, the strain-stress curve was corrected after taking into consideration the stiffness measured using the universal testing machine Instron.

3. Results

3.1. Microstructural characterization

The TiNbTa potential biomaterial for bone tissue replacement implants developed in this study showed in the XRD patterns two and three phases for the as-milled and as-sintered specimens, respectively (Fig. 1a). In both specimens, two structures were assigned, a body-centred cubic (*bcc*, *Im3m*) and a face-centred cubic (*fcc*, *Fm3m*) structure, designed as β and γ phases, respectively. Both structures were corroborated by comparison with the references files existing in the PDF4+ database for the *bcc*-Nb (80-2330) and *fcc*-Nb (34-0370), respectively.

Attending to the total absence of the corresponding peaks for Ti, Nb, and Ta raw materials and the complete solid solution between them

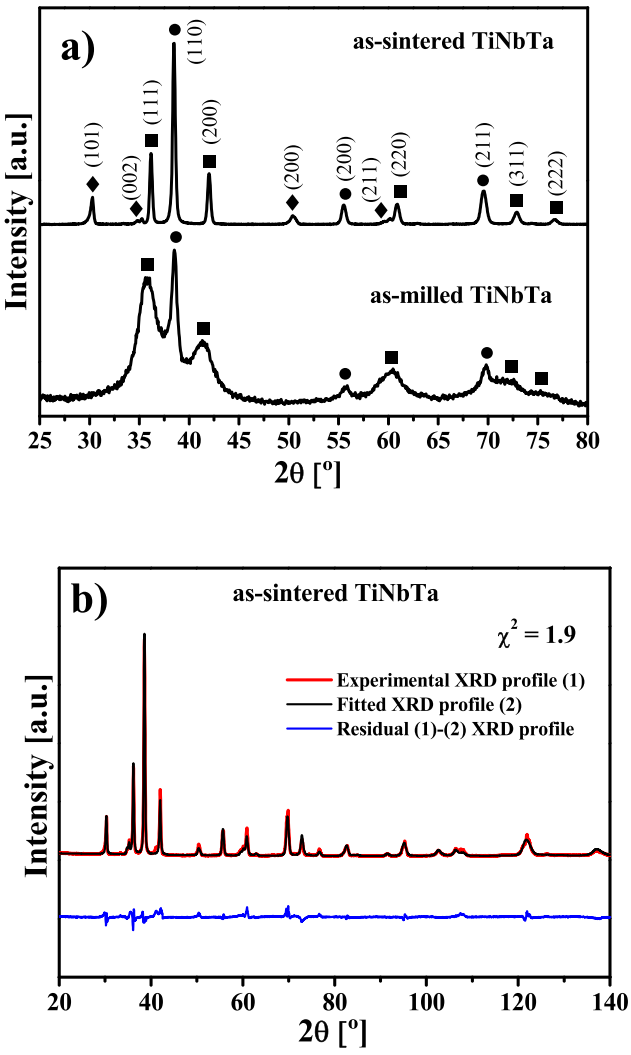

Fig. 1. a) X-ray powder diffraction patterns for the as-milled (down) and as-sintered (up) TiNbTa specimen. (●) β-TiNbTa (*bcc*, *Im-3m*); (■) γ-TiNbTa (*fcc*, *Fm-3m*); (◆) ZrO_2 (*tetragonal*, *P42/nmc*). b) Rietveld fitting for the as-sintered TiNbTa specimen.

[48], this aspect suggests both phases are to be two different TiNbTa ternary alloys or, at least, the TiNb, TiTa, and/or NbTa binary alloys. In addition, in the as-sintered TiNbTa specimen, small peaks corresponding to the zirconium oxide (ZrO_2, tetragonal, *P42/nmc*, reference number 50-1089) originating from the YSZ milling media were detected. The absence of these ZrO_2 peaks in the as-milled TiNbTa specimen suggests its total amorphization as consequence of the high milling time (60 h).

In both as-milled and as-sintered TiNbTa specimens, the lattice parameters (a, b, c), crystalline domain size (D) and percentage of phases were determined by Rietveld analysis. All values obtained are shown in Table 1. For comparison, the lattice parameters for elemental and milling media materials are also displayed in Table 1.

The lattice parameter for the phase with β (bcc) structure formed in the as-milled TiNbTa specimen was very close to those of β-Ti, β-Nb, and β-Ta, which were similar (Table 1). Then, the TiNbTa composition was not expected to greatly influence the lattice parameter of the β-phase. By comparison with the same β-phase for the as-sintered TiNbTa specimen, there was no displacement in the corresponding peaks (Fig. 1a). This aspect agrees with the same lattice parameters for the as-milled and as-sintered β-phase (Table 1). Therefore, for the β-phase, Ti, Nb, and Ta composition could be modified without changing their lattice parameters.

Table 1
Some microstructural characteristics for the as-milled and as-sintered TiNbTa specimens obtained by Rietveld analysis: lattice parameters (Å), crystalline domain size (D), and percentage of phases (wt%). For comparison, lattice parameters for pure elements and ZrO_2 are presented. Further, the Chi-Square Goodness of Fit parameter ($\chi 2$) is presented to corroborate the optimal Rietveld fitting. β: *bcc* structure; γ: *fcc* structure; N.D: Not detected.

Phase	Lattice parameters (Å)	D (nm)	Phases (wt%)	$\chi 2$
as-milled TiNbTa				
β-TiNbTa	a, b, c = 3.304	7.0	34	2.3
γ-TiNbTa	a, b, c = 4.361	2.4	66	
ZrO_2	N.D.	N.D.	N.D.	
as-sintered TiNbTa				
β-TiNbTa	a, b, c = 3.305	320	42	1.9
γ-TiNbTa	a, b, c = 4.297	360	47	
ZrO_2	a, b = 3.598 c = 5.152	250	11	
Pure elements				
β-Ti	a, b, c = 3.307	–	–	–
β-Nb	a, b, c = 3.303	–	–	
β-Ta	a, b, c = 3.306	–	–	
γ-Nb [44]	a, b, c = 4.280	–	–	
ZrO_2	a, b = 3.598 c = 5.152	–	–	

In contrast, the γ-phase (*fcc*) underwent a change in the lattice parameters from the metastable γ-Nb [44] to as-sintered TiNbTa (Table 1). Initially, the increase of the lattice parameter for the as-milled TiNbTa suggested the introduction of Ti and Ta in the γ-Nb. Subsequently, for the as-sintered TiNbTa, the diminishing of the lattice parameter can be attributed to the inverse behavior in the γ-Nb, due to its metastable characteristic. This last observation was consistent with the higher 2θ displacements in the corresponding XRD patters (Fig. 1a). Therefore, the formation of a Ti, Nb, and Ta substitutional solid solution leads to a higher lattice parameter from γ-Nb (a, b, c = 4.280 Å) to as-milled TiNbTa (a, b, c = 4.361 Å) and lower lattice parameter for as-sintered TiNbTa (a, b, c = 4.297 Å). In addition, it could be determined the lattice parameter for the ZrO_2 coming from the YSZ milling media. This value matched exactly with the value provided in the PDF 4 + database, corroborating the presence of ZrO_2 in the as-sintered TiNbTa specimen.

With regard to the crystalline domain size (D), submicrometric value was observed for all phases, even for the as-sintered TiNbTa. Thus, one of the goals of this study was achieved, i.e., the development of a submicrometric structured alloy, which have higher mechanical strength than microstructured alloys [49] (Table 1).

The Rietveld analysis carried out on XRD pattern of (Fig. 1a) revealed the weight percentage of phases (Table 1). The goodness of fit parameter (χ^2) for the Rietveld refinement was close to two, which it is a typical value for optimal fitting (Table 1). As corroboration, the fitted XRD by Rietveld for the as-sintered TiNbTa specimen is showed in Fig. 1b. Thus, it was observed that the percentage of the γ-phase was reduced, while that of the β-phase was increased from as-milled to as-sintered TiNbTa specimens. This suggests a partial transformation of the *fcc* to *bcc* microstructure during sintering. The metastable character of the developed γ-phase is expected to be analogous to the metastable γ-Nb allotropic phase [44]. The ZrO_2 amount from YSZ milling media was also determined for the as-sintered TiNbTa specimen due to the total absence of the characteristic peaks for ZrO_2 XRD pattern in the as-milled TiNbTa specimen, as consequence of its amorphization. Thus, the ZrO_2 amount attributable to the milling media was 11 wt% (Table 1).

SEM images were obtained for the as-sintered TiNbTa specimen. It was observable a practically total absence of porosity, suggesting a full densification of the sintered specimen. This as-sintered TiNbTa specimen showed an interesting submicrometric structure, as shown in Fig. 2. The exceptionally high heating rate applied (500 °C·min^{-1}) during PECS allowed the retention of the submicrometric size for all particles after sintering. This complete structure developed is a very positive achievement related to the osseointegration, i.e., the direct structural and functional connection between living bone and the surface of a load-bearing implant [50]. In practice, this structure developed for the as-sintered TiNbTa specimen is a positive effect that can directly enhance cell behavior at an early stage and in the long-term osseointegration of the implant [51,52].

In relation to the microstructure observed by SEM, three different zones were detected (see Fig. 2), with each of them showing different contrasts. Zone 1 was composed for an apparently continuous light-grey phase (it was not observed the grain boundaries for this phase) and submicrometric (<500 nm) dark grey particles. Other smaller white particles were exceptionally detected (marked by a white square). The compositions of both grey particles were semiquantitatively determined by SEM-EDS (Table 2). The dark grey particles (marked with "d" in the zone 1 of Fig. 2) presented an average atomic composition of 75Ti-17Nb-8Ta. In turn, the light-grey phase (marked with "l" in the zone 1 of Fig. 2) possessed a composition of 40Ti-43Nb-17Ta. These compositions showed a higher Ti percentage phase and another with higher Ta and Nb percentage than the 57Ti-30Nb-13Ta nominal atomic percentage, respectively. Therefore, it is expected that these two corroborated TiNbTa alloys remain from the corresponding as-milled TiNbTa specimen to the as-sintered TiNbTa (β and γ phases, observed by XRD). The compositions of the smallest white particles were impossible to determine due to their extremely small size (<100 nm).

Zones 2 and 3 (Fig. 2) showed two and three contrasts, respectively. As it was in the zone 1, the composition of these zones could not be determined due to the extremely small size of the submicrometric particles. In addition, by comparison with the number of phases detected by XRD (Fig. 1a), it is suggested that the particles shown in the three zones of Fig. 2 are in fact the β-TiNbTa (*bcc*) and the γ-TiNbTa (*fcc*) phases, with different particle sizes and distribution, due to the heterogeneous heat treatment generated by PECS. With regard to the smallest particles with lightest contrast existing in zones 1 and 3 (Fig. 2, marked by white squares), they must correspond to the ZrO_2 originating from the YSZ milling media, as the third phase determined by XRD.

This developed submicrometric nature is a typical characteristic for materials developed by the PECS sintering method [53,54]. The particles thus obtained are interesting due to the expected higher mechanical strength of nano and submicrometric structured materials in comparison with microstructured specimens, as consequence of the known Hall-Petch behavior that has been reported in some biomaterials [55]. This effect is presented for crystal sizes higher than a nanometric critical size (around 30–10 nm), when the reported inverse Hall-Petch behaviour takes place [56].

The general SEM-EDS analysis were carried out on the full-polished surface of the as-sintered TiNbTa specimen, yielding a 59Ti-29Nb-12Ta relative at.%. This composition was close to the nominal 57Ti-30Nb-13Ta, corroborating the optimal measurements of EDS and the absence of the migration of metal out to the PECS die, which is typical for metal pressure-assisted sintering methods [57]. In turn, the absolute Zr at.% obtained for the same general EDS-SEM analysis was 6 at.%. This value is consistent with the general weight percentage obtained by Rietveld (11 wt% of ZrO_2).

On the other hand, it is necessary to emphasize that no C and a low O amount (lower than 2 wt%) were determined by EDS. The decomposition of the PCA (Stearic acid, 3 wt%) during sintering, had to produce typical volatile reaction products for organic acids, such as CO_2 and H_2O leaving the as-sintered TiNbTa specimen before full densification. Moreover, the lower O amount determined was in agreement with the amount of ZrO_2 from milling media.

Subsequently, to clarify and corroborate the composition of phases, a high-angle annular dark-field image (HAADF) was obtained in the TEM, and a mapping-EDS was collected (Fig. 3). The mapping-EDS was collected in the zone 2, which was impossible to obtain by SEM-EDS. It clearly showed two different phases. The first one (marked as "A" in Fig. 3) was associated to the higher Ti amount (red color in Fig. 3); in

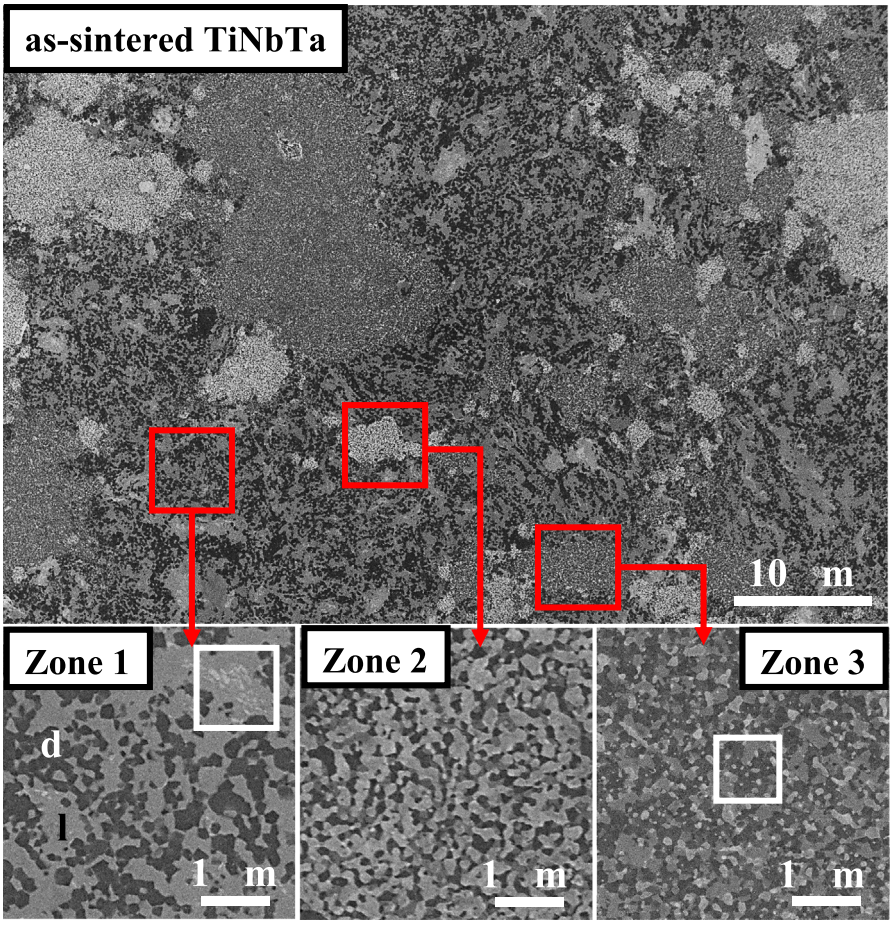

Fig. 2. Low-magnification SEM image for the as-sintered TiNbTa specimen showing general morphology, microstructure, and distribution of phases. High-magnification SEM images showing the three different zones, marked by red squares. "d" and "l" correspond to the SEM-EDS measurements for dark and light particles of zone 1. White squares: The smallest white particles detected.

this phase, the brightness for Nb (green) and Ta (blue) was low, suggesting a high Ti content, according to the first alloy determined previously by SEM-EDS, i.e., the 75Ti-17Nb-8Ta alloy. On the other hand, Nb and Ta are associated mostly with the second phase (marked as "B" in the Fig. 3), when Ti was in low amount. This phase could be matched to the abovementioned 40Ti-43Nb-17Ta alloy. The Zr was detected in some points, and it is not associated with Ti, Nb, and Ta, suggesting that the ZrO_2 from YSZ remains unalloyed.

The semiquantitative STEM-EDS determination of both TiNbTa alloys was carried out on areas #1 and #2 marked in Fig. 3, yielding results similar to those obtained by SEM-EDS (Table 2), thereby corroborating that the two *fcc* and *bcc* are, in fact, TiNbTa alloys. Thus, the β-TiNbTa is the desired microstructure due to its expected low Young's modulus in comparison with α-Ti alloys. The stabilizations of this beta phase at room temperature was possible due to the reported β stabilizing characteristic of Nb and Ta, as expected. However, in this case, another Ti alloy determined, the γ-TiNbTa, can be asserted as a novel and interesting candidate in the development of Ti alloys for biomedical applications, since γ-Ti alloys have not been reported hitherto. In this sense, it is interesting to note that although there is a complete binary miscibility between Ti, Nb, and Ta in the solid state, attending to the corresponding binary phase diagrams [48], the excessive addition of Nb causes the formation of the γ-TiNbTa, from the γ-Nb allotropic structure [44].

Table 2
General, zone 1 and zone 2 semiquantitative EDS compositions (at.%) for the as-sintered TiNbTa specimen.

Zone		Ti	Nb	Ta	Zr
SEM-EDS					
General		54 ± 3	28 ± 3	12 ± 2	6 ± 2
Zone 1	Dark contrast	75 ± 3	17 ± 3	8 ± 2	0
	Light contrast	40 ± 4	43 ± 3	17 ± 3	0
TEM-EDS					
Zone 2	Crystal A	72 ± 3	19 ± 3	9 ± 3	0
	Crystal B	43 ± 2	41 ± 4	16 ± 3	0

The next step in this work was to connect the β-TiNbTa and the γ-TiNbTa phases developed with each TiNbTa composition determined. For this purpose, the structures of the "A" and "B" crystals exposed in Fig. 3 were elucidated by SAED (Fig. 4). Contrary to expectation, the γ-TiNbTa alloy (crystal "A") was assigned to the Ti richer alloy (75Ti-17Nb-8Ta). This assertion was corroborated by two SAED patterns oriented along the [101] and [001] zone axes. Thus, the development of a novel γ-Ti alloy was also corroborated by SAED. Thus far, only α-Ti and β-Ti alloys had been developed. Synergy effects could have caused this γ-Ti alloy formation. The introduction of a high amount of alloying elements (Nb and Ta) together with the energy transferred during milling could have led to the deformation and formation of a new phase, as it was detected for the as-milled specimen. Thereafter, the high heating rate used during PECS sintering (500 °C·min^{-1}) prevented the total transformation of this γ-TiNbTa to the expected β-TiNbTa, according to the phase diagrams [48].

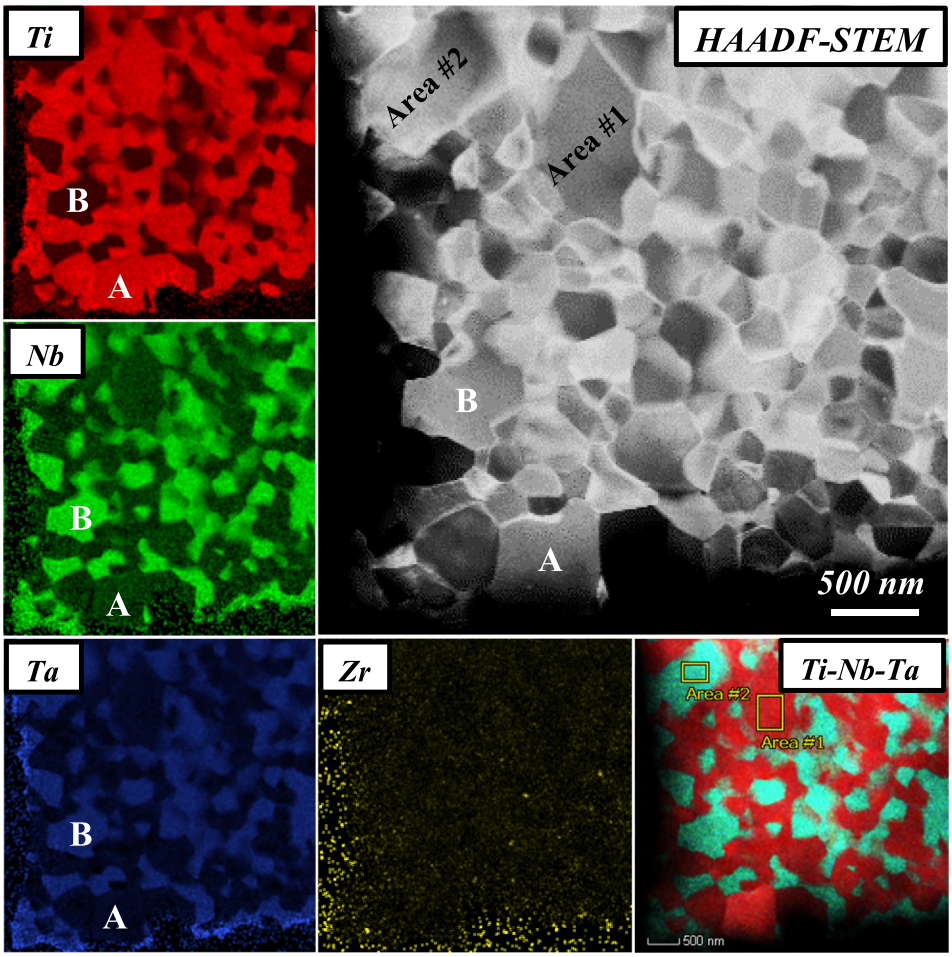

Fig. 3. HAADF image obtained by STEM, corresponding to the zone 2 (Fig. 1), showing the submicrometric alloy. Mapping STEM-EDS was displayed with the Ti, Nb, Ta and Zr elements. Compositions of Area #1: 72Ti-19Nb-9Ta; Area #2: 43Ti-41Nb-16Ta. A and B are the crystals used in Fig. 4 to determine the crystallography structure of phases.

On the other hand, the "B" crystal (shown in Fig. 4 and also marked in Fig. 3) presented the typical β-TiNbTa structure, with the composition of the abovementioned β-40Ti-43Nb-17Ta. The lower Ti amount introduced in this β-TiNbTa did not cause any structural transformation, retaining the stable *bcc* structure, and the stable structure for Nb and Ta at room temperature. In this case, this assertion was made on the basis of two SAED patterns oriented along the [113] and [001] zone axes (Fig. 4).

3.2. Mechanical behavior

Once the microstructure was elucidated, the mechanical performance of the specimen, particularly, the Young's modulus and the yield strength, were determined by the compression test according to the ASTM E9-09. Fig. 5a displays the strain-stress curve obtained. The first assertion can made about the Young's modulus obtained from the slopes, 49 ± 3 GPa. This value was lower than those of c.p. Ti and Ti6Al4V [2] and even lower than those of other β-TiNbTa-based alloys obtained by cast (from 55 to 91 GPa) [19] and for the widely extended β-TiNb-based alloys (60–110 GPa, approximately [6,58]). However, it must be taken into account that about 6 at.% of the specimen was attributable to YSZ originating from the milling media. The base of YSZ is ZrO_2 with a Young's modulus of 205 GPa [59]. Thus, according to the volumetric mixing law, the final E from the as-sintered TiNbTa specimen developed in this work would be reduced when another milling media would be used. Furthermore, the low value of E obtained could be a direct consequence of the existence of new γ-TiNbTa, instead of only β-TiNbTa, since E for *fcc* has been reported to be lower than that for *bcc* alloy structures [60,61]. In addition, Zhu [62] showed how the Young's modulus of nanocrystalline materials decreases with the reduction of the grain size to the nanoscale.

Another outstanding achievement was the exceptionally higher yield strength expected for the developed (β + γ)-TiNbTa specimen (>1860 MPa), in comparison with the c.p. Ti (480–552 MPa) [14], Ti6Al4V (880 MPa) [14] and also the β-Ti alloys, with values of 600–800 MPa for the most promising β-Ti-based alloys [19,33,63]. It is important to note that despite the high maximum load applied (100 kN) and small size of the specimens (θ = 8 mm and h = 10 mm), it was impossible to reach the yield strength point. This is a very important achievement since the yield strength is another essential Ti alloys parameter used for implants to accommodate the compression, tension, and torsion stress state, which may be experienced by the implants used in the human body [19,33].

All the achievements mentioned above are very important since they allow the use of this (β + γ)-TiNbTa as raw material for the preparation of Ti-based foams. This would introduce a high amount of porosity to reduce the Young's modulus without a detrimental effect on the yield strength. Fig. 5b shows the estimation of Young's modulus and the yield strength by the introduction of porosity in the (β + γ)-TiNbTa,

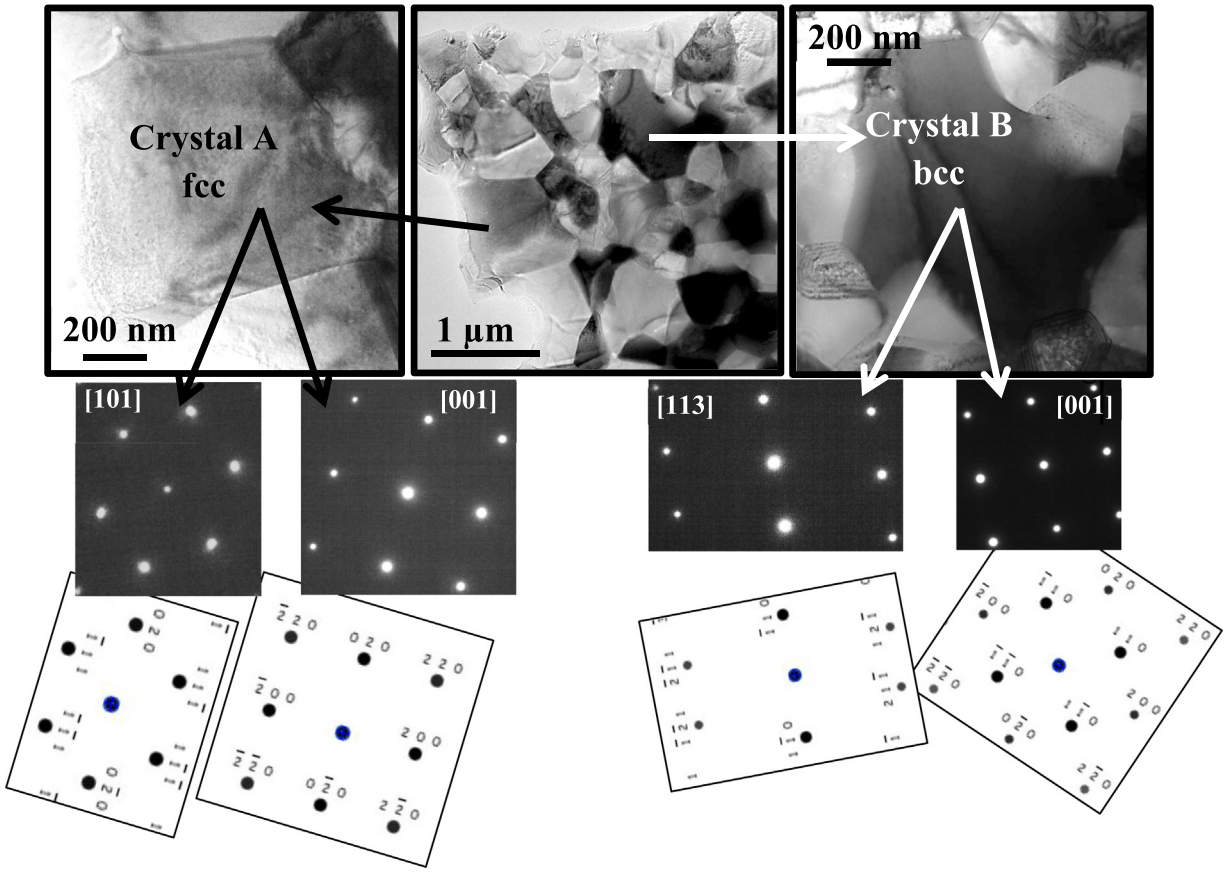

Fig. 4. TEM images of zone 2, showing two crystals (A and B, also marked in Fig. 2) and the corresponding SAED patterns and the indexed crystallographic planes. Crystal A (TiNbTa with higher Ti content): *fcc* structure and *Fm3m* SGS. Crystal B (TiNbTa with lower Ti content): *bcc* structure and *Im3m* SGS.

according to the Mondal (1) [64], Knudsen (2) [65], and Ryshkewitch (3) [66] equations:

$$E_P/E_0 = (1-P)^2/(1+yP); y = 2-3v_0 \quad (1)$$

$$E_P/E_0 = \exp(-mP) \quad (2,\ 3)$$

where E_P and E_0 are the elastic modulus for the foam and the bulk Ti alloys, respectively. P is the porosity amount of the foam. υ_0 is the Poissons ratio for the bulk Ti alloys. Finally, m is an experimental parameter equals to 3.95 and 7 for Knudsen and Ryshkewitch, respectively.

Thus, as shown in Fig. 5b, it would be possible to develop a submicrometric ($\beta + \gamma$)-TiNbTa foam with the lowest Young's modulus obtained until now (as example, 12 GPa for 20 vol% of porosity) and an estimated yield strength of ~460 MPa, according to the Ryshkewitch equation. This σ_y value is much higher than that of the cortical bone (170–227 MPa), as determined by the compression test in different human bones [67–69]), and, consequently, also for the trabecular bone.

Similar assertions can be obtained using the Mondal and Knudsen equations. Further, in these cases, low E with values close to those of the trabecular bone could be reached with higher volume of porosity (11 GPa and 7 GPa for 50 vol% of porosity. Fig. 5b). Correspondingly, the yield strength (419 MPa and 258 MPa) would be higher than those of the trabecular bone as well as the cortical bone. In addition, the possibility of introducing a high level of porosity would increase the open porosity percentage and, consequently, also improving the ingrowth bone cells into the implants and, finally, improving osseointegration [70,71]. In this context, it is important to emphasize the present work is the basis to develop novel γ-TiNbTa foams with improved mechanical behavior than usual α-Ti and β-Ti alloy foams by the space holder technique, which the authors are fabricating at this moment.

4. Conclusions

- By applying a combination of LEMA and PECS powder metallurgy processes, it was successfully developed a novel TiNbTa material with interesting microstructural and mechanical characteristics that make it suitable for bone replacements implants.
- The microstructure developed showed different zones with different particle sizes, but always in the submicrometric range.
- In all zones detected for the novel TiNbTa material, two Ti-based alloys were observed. The first one was the typical β-TiNbTa alloy with *bcc* structure and a lower Ti atomic amount (40Ti-43Nb-17Ta) than usual. However, the second was a novel γ-TiNbTa alloy with *fcc* structure and a higher Ti atomic percentage (75Ti-17Nb-8Ta).
- All characteristics for the novel TiNbTa material developed, including its submicrometric structure, low Young's modulus, β-TiNbTa (*bcc* structure), and novel γ-TiNbTa (*fcc* structure), confers on it the combined advantages of one of the lowest Young's modulus (49 ± 3 GPa) and an outstanding yield strength (>1860 MPa), which has not been previously reported for bulk Ti-based biomaterials.
- The outstanding yield strength for the novel ($\gamma + \beta$)-TiNbTa material developed would allow the fabrication of ($\gamma + \beta$)-TiNbTa foams with high porosity amount, reaching Young's modulus similar and yield strength higher to the corresponding for cortical and trabecular bones, as it was determined by the reported Knudsen, Mondal, and Ryshkewitch equations. Therefore, it would be possible to eliminate the undesirable *stress-shielding* phenomenon with the use of this material.

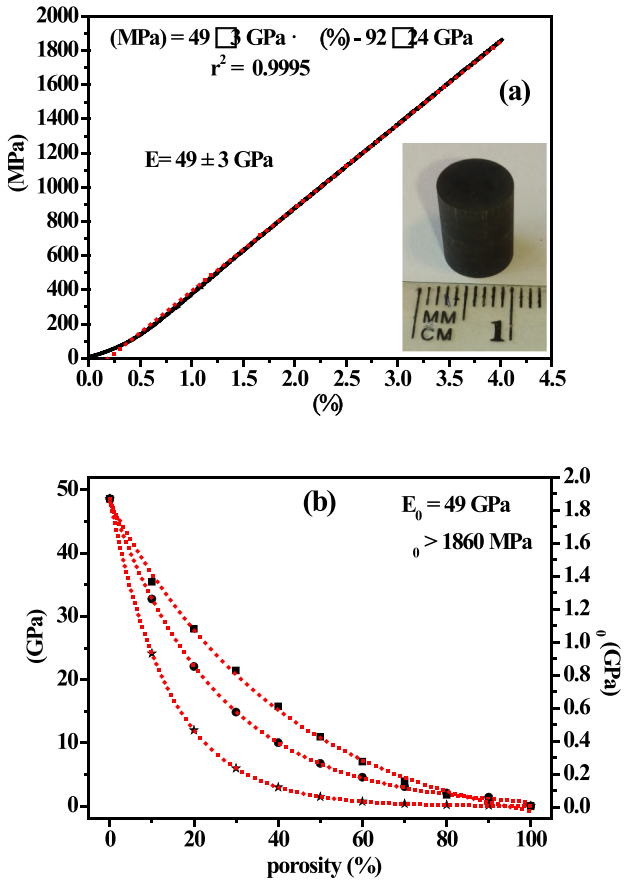

Fig. 5. a) Strain-stress curve for the TiNbTa potential biomaterial, determined by compression test until 100 kN maximum load. Inset: A representative specimen tested (θ = 8 mm and h = 10 mm). b) Estimated Young's modulus (E) and Yield strength (σ_0) using the Mondal (■), Knudsen (•) and Ryshkewitch (★) equations for all the range of porosity to form foams and starting from experimental data at porosity equal to 0 (E_0 = 49 GPa and σ_{y0} = 1860 MPa).

Acknowledgments

This work was supported under postdoctoral grant No. 3150060, which is financed by the FONDECYT fund (Government of Chile). Authors want to thanks to the University of Seville for the use of its general research service (CITIUS) under the grant no. 2017/833 and to the Nanomaterials and Nanotechnology Research Center (CINN-CSIC-UNIOVI) for the availability of the PECS device.

References

[1] J.R. da Silva, A. Castellano, J.P.M. Barbosa, L.F. Gil, C. Marin, R. Granato, E.A. Bonfante, N. Tovar, M.N. Janal, P.G. Coelho, Histomorphological and histomorphometric analyses of grade IV commercially pure titanium and grade V Ti-6Al-4V titanium alloy implant substrates: an in vivo study in dogs, Implant. Dent. 25 (5) (2016) 650–655.
[2] J. Breme, E. Eisenbarth, V. Biehl, Titanium and its alloys for medical applications, Titanium and Titanium Alloys, Wiley-VCH Verlag GmbH & Co. KGaA 2005, pp. 423–451.
[3] J.Y. Rho, R.B. Ashman, C.H. Turner, Young's modulus of trabecular and cortical bone material: ultrasonic and microtensile measurements, J. Biomech. 26 (2) (1993) 111–119.
[4] M. Ridzwan, S. Shuib, A. Hassan, A. Shokri, M.M. Ibrahim, Problem of stress shielding and improvement to the hip implant designs: a review, J. Med. Sci. 7 (3) (2007) 460–467.
[5] H. Ibrahim, S.N. Esfahani, B. Poorganji, D. Dean, M. Elahinia, Resorbable bone fixation alloys, forming, and post-fabrication treatments, Mater. Sci. Eng. C 70 ((2017) 870–888.
[6] M. Niinomi, Y. Liu, M. Nakai, H. Liu, H. Li, Biomedical titanium alloys with Young's moduli close to that of cortical bone, Regenerative Biomaterials 3 (3) (2016) 173–185.
[7] B. Helgason, E. Perilli, E. Schileo, F. Taddei, S. Brynjolfsson, M. Viceconti, Mathematical relationships between bone density and mechanical properties: a literature review, Clin. Biomech. 23 (2) (2008) 135–146.
[8] D.P. Mondal, J.D. Majumder, N. Jha, A. Badkul, S. Das, A. Patel, G. Gupta, Titanium-cenosphere syntactic foam made through powder metallurgy route, Mater. Des. 34 (2012) 82–89.
[9] Z. Esen, S. Bor, Characterization of Ti-6Al-4V alloy foams synthesized by space holder technique, Mater. Sci. Eng. A 528 (7–8) (2011) 3200–3209.
[10] Y. Torres, P. Trueba, J. Pavon, I. Montealegre, J.A. Rodriguez-Ortiz, Designing, processing and characterisation of titanium cylinders with graded porosity: an alternative to stress-shielding solutions, Mater. Des. 63 (2014) 316–324.
[11] Y. Torres, P. Trueba, J.J. Pavon, E. Chicardi, P. Kamm, F. Garcia-Moreno, J.A. Rodriguez-Ortiz, Design, processing and characterization of titanium with radial graded porosity for bone implants, Mater. Des. 110 (2016) 179–187.
[12] S. Bernard, V.K. Balla, S. Bose, A. Bandyopadhyay, Compression fatigue behavior of laser processed porous NiTi alloy, J. Mech. Behav. Biomed. Mater. 13 (2012) 62–68.
[13] E.E. Asik, S. Bor, Fatigue behavior of Ti-6Al-4V foams processed by magnesium space holder technique, Mater. Sci. Eng. A 621 (2015) 157–165.
[14] ASTM, ASTM B265-15. Standard Specification for Titanium and Titanium Alloy Strip, Sheet, and Plate, 2015.
[15] S. KASHEF, J. LIN, P.D. HODGSON, W. YAN, Mechanical properties of titanium foam for biomedical applications, Int. J. Mod. Phys. B 22 (31n32) (2008) 6155–6160.
[16] H.H. Bayraktar, E.F. Morgan, G.L. Niebur, G.E. Morris, E.K. Wong, T.M. Keaveny, Comparison of the elastic and yield properties of human femoral trabecular and cortical bone tissue, J. Biomech. 37 (1) (2004) 27–35.
[17] I. Halevy, G. Zamir, M. Winterrose, G. Sanjit, G. Carlos Roberto, M.-G. Ariel, Crystallographic structure of Ti-6Al-4V, Ti-HP and Ti-CP under high-pressure, J. Phys. Conf. Ser. 215 (1) (2010), 012013. .
[18] M. Niinomi, M. Nakai, J. Hieda, Development of new metallic alloys for biomedical applications, Acta Biomater. 8 (11) (2012) 3888–3903.
[19] M. Geetha, A.K. Singh, R. Asokamani, A.K. Gogia, Ti based biomaterials, the ultimate choice for orthopaedic implants – a review, Prog. Mater. Sci. 54 (3) (2009) 397–425.
[20] S. Bahl, S. Das, S. Suwas, K. Chatterjee, Engineering the next-generation tin containing beta titanium alloys with high strength and low modulus for orthopedic applications, J. Mech. Behav. Biomed. Mater. 78 (2018) 124–133.
[21] I. Kopova, J. Strasky, P. Harcuba, M. Landa, M. Janecek, L. Bacakova, Newly developed Ti-Nb-Zr-Ta-Si-Fe biomedical beta titanium alloys with increased strength and enhanced biocompatibility, Mater. Sci. Eng. C 60 (2016) 230–238.
[22] M. Peters, J. Hemptenmacher, J. Kumpfert, C. Leyens, Structure and Properties of Titanium and Titanium Alloys, Titanium and Titanium Alloys, Wiley-VCH Verlag GmbH & Co. KGaA, 2005 1–36.
[23] R. Salloom, R. Banerjee, S.G. Srinivasan, Effect of beta-stabilizer elements on stacking faults energies and ductility of alpha-titanium using first-principles calculations, J. Appl. Phys. 120 (17) (2016) 8.
[24] S. Ehtemam-Haghighi, K.G. Prashanth, H. Attar, A.K. Chaubey, G.H. Cao, L.C. Zhang, Evaluation of mechanical and wear properties of TixNb7Fe alloys designed for biomedical applications, Mater. Des. 111 (2016) 592–599.
[25] I.V. Okulov, A.S. Volegov, H. Attar, M. Bönisch, S. Ehtemam-Haghighi, M. Calin, J. Eckert, Composition optimization of low modulus and high-strength TiNb-based alloys for biomedical applications, J. Mech. Behav. Biomed. Mater. 65 (2017) 866–871.
[26] K. Cho, M. Niinomi, M. Nakai, J. Hieda, Y. Kawasaki, Development of high modulus Ti-Fe-Cu alloys for biomedical applications, Mater. Trans. 54 (4) (2013) 574–581.
[27] M. Kikuchi, M. Takahashi, O. Okuno, Elastic moduli of cast Ti–Au, Ti–Ag, and Ti–Cu alloys, Dent. Mater. 22 (7) (2006) 641–646.
[28] J. She, Y.Z. Zhan, High volume intermetallics reinforced Ti-based composites in situ synthesized from Ti-Si-Sn ternary system, Mater. Sci. Eng. A 528 (10−11) (2011) 3871–3875.
[29] S. Guo, Q.K. Meng, X.Q. Zhao, Q.M. Wei, H.B. Xu, Design and fabrication of a metastable beta-type titanium alloy with ultralow elastic modulus and high strength, Sci. Rep. 5 (2015) 8.
[30] M. Tane, S. Akita, T. Nakano, K. Hagihara, Y. Umakoshi, M. Niinomi, H. Nakajima, Peculiar elastic behavior of Ti-Nb-Ta-Zr single crystals, Acta Mater. 56 (12) (2008) 2856–2863.
[31] D. Raabe, B. Sander, M. Friák, D. Ma, J. Neugebauer, Theory-guided bottom-up design of β-titanium alloys as biomaterials based on first principles calculations: theory and experiments, Acta Mater. 55 (13) (2007) 4475–4487.
[32] S.-j. Dai, Y. Wang, F. Chen, X.-q. Yu, Y.-f. Zhang, Design of new biomedical titanium alloy based on d-electron alloy design theory and JMatPro software, Trans. Nonferrous Metals Soc. China 23 (10) (2013) 3027–3032.
[33] D. Kuroda, M. Niinomi, M. Morinaga, Y. Kato, T. Yashiro, Design and mechanical properties of new beta type titanium alloys for implant materials, Mater. Sci. Eng. A 243 (1–2) (1998) 244–249.
[34] E. Chicardi, C. Garcia-Garrido, M.J. Sayagues, Y. Torres, V. Amigo, C. Aguilar, Development of a novel fcc structure for an amorphous-nanocrystalline Ti-33Nb-4Mn (at.%) ternary alloy, Mater. Charact. 135 (2018) 46–56.
[35] A. Inoue, W. Zhang, T. Zhang, K. Kurosaka, High-strength Cu-based bulk glassy alloys in Cu–Zr–Ti and Cu–Hf–Ti ternary systems, Acta Mater. 49 (14) (2001) 2645–2652.
[36] A. Inoue, C. Fan, J. Saida, T. Zhang, High-strength Zr-based bulk amorphous alloys containing nanocrystalline and nanoquasicrystalline particles, Sci. Technol. Adv. Mater. 1 (2) (2000) 73–86.
[37] T.G. Nieh, J. Wadsworth, Hall-Petch relation in nanocrystalline solids, Scr. Met. Mater. 25 (4) (1991) 955–958.
[38] Z.P. Wan, Y. Sun, L.X. Hu, H. Yu, Experimental study and numerical simulation of dynamic recrystallization behavior of TiAl-based alloy, Mater. Des. 122 (2017) 11–20.
[39] C. Suryanarayana, Mechanical alloying and milling, Prog. Mater. Sci. 46 (1–2) (2001) 1–184.

[40] Z.A. Munir, U. Anselmi-Tamburini, M. Ohyanagi, The effect of electric field and pressure on the synthesis and consolidation of materials: a review of the spark plasma sintering method, J. Mater. Sci. 41 (3) (2006) 763–777.
[41] H. Matsuno, A. Yokoyama, F. Watari, M. Uo, T. Kawasaki, Biocompatibility and osteogenesis of refractory metal implants, titanium, hafnium, niobium, tantalum and rhenium, Biomaterials 22 (11) (2001) 1253–1262.
[42] A.H. Hussein, M.A.H. Gepreel, M.K. Gouda, A.M. Hefnawy, S.H. Kandil, Biocompatibility of new Ti-Nb-Ta base alloys, Mater. Sci. Eng. C 61 (2016) 574–578.
[43] E. Chicardi, F.J. Gotor, V. Medri, S. Guicciardi, S. Lascano, J.M. Cordoba, Hot-pressing of (Ti,Mt)(C,N)-Co-Mo2C (Mt = Ta,Nb) powdered cermets synthesized by a mechanically induced self-sustaining reaction, Chem. Eng. J. 292 (2016) 51–61.
[44] P.P. Chattopadhyay, S.K. Pabi, I. Manna, A metastable allotropic transformation in Nb induced by planetary ball milling, Mater. Sci. Eng. A 304 (2001) 424–428.
[45] C. Salvo, C. Aguilar, R. Cardoso-Gil, A. Medina, L. Bejar, R.V. Mangalaraja, Study on the microstructural evolution of Ti-Nb based alloy obtained by high-energy ball milling, J. Alloys Compd. 720 (2017) 254–263.
[46] A. Boultif, D. Louer, Powder pattern indexing with the dichotomy method, J. Appl. Crystallogr. 37 (2004) 724–731.
[47] J. Rodríguez-Carvajal, Recent developments of the program FULLPROF, commission on powder diffraction (IUCr), Newsletter 26 (2001) 12–19.
[48] H. Okamoto, M.E. Schlesinger, E.M. Mueller, Alloy Phase Diagrams, 2016.
[49] Z.C. Cordero, B.E. Knight, C.A. Schuh, Six decades of the Hall-Petch effect - a survey of grain-size strengthening studies on pure metals, Int. Mater. Rev. 61 (8) (2016) 495–512.
[50] T. Albrektsson, P.I. Branemark, H.A. Hansson, J. Lindstrom, Osseointegrated titanium implants - requirements for ensuring a long-lasting, direct bone-to-implant anchorage in man, Acta Orthop. Scand. 52 (2) (1981) 155–170.
[51] R.A. Gittens, R. Olivares-Navarrete, Z. Schwartz, B.D. Boyan, Implant osseointegration and the role of microroughness and nanostructures: lessons for spine implants, Acta Biomater. 10 (8) (2014) 3363–3371.
[52] L. Salou, A. Hoornaert, G. Louarn, P. Layrolle, Enhanced osseointegration of titanium implants with nanostructured surfaces: an experimental study in rabbits, Acta Biomater. 11 (2015) 494–502.
[53] A.A. Chaudhry, H.X. Yan, K.N. Gong, F. Inam, G. Viola, M.J. Reece, J.B.M. Goodall, I.U. Rehman, F.K. McNeil-Watson, J.C.W. Corbett, J.C. Knowles, J.A. Darr, High-strength nanograined and translucent hydroxyapatite monoliths via continuous hydrothermal synthesis and optimized spark plasma sintering, Acta Biomater. 7 (2) (2011) 791–799.
[54] D. Grossin, S. Rollin-Martinet, C. Estournes, F. Rossignol, E. Champion, C. Combes, C. Rey, C. Geoffroy, C. Drouet, Biomimetic apatite sintered at very low temperature by spark plasma sintering: physico-chemistry and microstructure aspects, Acta Biomater. 6 (2) (2010) 577–585.
[55] S.V. Muley, A.N. Vidvans, G.P. Chaudhari, S. Udainiya, An assessment of ultra fine grained 316L stainless steel for implant applications, Acta Biomater. 30 (2016) 408–419.
[56] H. Conrad, J. Narayan, On the grain size softening in nanocrystalline materials, Scr. Mater. 42 (11) (2000) 1025–1030.
[57] J.M. Cordoba, E. Chicardi, R. Poyato, F.J. Gotor, V. Medri, S. Guicciardi, C. Melandri, Spark plasma sintering of TixTa1-xC0.5N0.5-based cermets: effects of processing conditions on chemistry, microstructure and mechanical properties, Chem. Eng. J. 230 (2013) 558–566.
[58] T. Ozaki, H. Matsumoto, S. Watanabe, S. Hanada, Beta Ti alloys with low Young's Modulus, Mater. Trans. 45 (8) (2004) 2776–2779.
[59] G. Berg, C. Friedrich, E. Broszeit, C. Berger, Data collection of properties of hard material, Handbook of Ceramic Hard Materials, Wiley-VCH Verlag GmbH 2008, pp. 965–995.
[60] F. Povolo, H.O. Mosca, Zener relaxation strength in b.c.c. and f.c.c. alloys under torsional and longitudinal excitations, Acta Metall. Mater. 42 (1) (1994) 109–117.
[61] H. Diao, X. Xie, F. Sun, K.A. Dahmen, P.K. Liaw, Mechanical properties of high-entropy alloys, in: M.C. Gao, J.-W. Yeh, P.K. Liaw, Y. Zhang (Eds.),High-Entropy Alloys: Fundamentals and Applications, Springer International Publishing, Cham 2016, pp. 181–236.
[62] L. Zhu, X. Zheng, Influence of interface energy and grain boundary on the elastic modulus of nanocrystalline materials, Acta Mech. 213 (3) (2010) 223–234.
[63] W.F. Ho, C.P. Ju, J.H. Chern Lin, Structure and properties of cast binary Ti–Mo alloys, Biomaterials 20 (22) (1999) 2115–2122.
[64] D.P. Mondal, N. Ramakrishnan, K.S. Suresh, S. Das, On the moduli of closed-cell aluminum foam, Scr. Mater. 57 (10) (2007) 929–932.
[65] F.P. Knudsen, Effect of porosity on young modulus of alumina, J. Am. Ceram. Soc. 45 (2) (1962) 94–95.
[66] E. Ryshkewitch, Compression strength of porous sintered alumina and zirconia, J. Am. Ceram. Soc. 36 (2) (1953) 65–68.
[67] P. Zioupos, J.D. Currey, Changes in the stiffness, strength, and toughness of human cortical bone with age, Bone 22 (1) (1998) 57–66.
[68] F.G. Evans, Mechanical-properties and histology of cortical bone from younger and older men, Anat. Rec. 185 (1) (1976) 1–12.
[69] B.K. Hall, Part I. Vertebrate Skeletal Tissues, Bones and Cartilage, Second Edition Academic Press, San Diego, 2015 1.
[70] H.L. Li, S.M. Oppenheimer, S.I. Stupp, D.C. Dunand, L.C. Brinson, Effects of pore morphology and bone ingrowth on mechanical properties of microporous titanium as an orthopaedic implant material, Mater. Trans. 45 (4) (2004) 1124–1131.
[71] R.M. Wazen, L.P. Lefebvre, E. Baril, A. Nanci, Initial evaluation of bone ingrowth into a novel porous titanium coating, J. Biomed. Mater. Res., Part B 94B (1) (2010) 64–71.